Q. J. R. Meteorol. Soc. (1999), **125**, pp. 1107–1127

The influence of cross-equatorial pressure gradients on the location of near-equatorial convection

By ROBERT A. TOMAS[1]*, JAMES R. HOLTON[2] and PETER J. WEBSTER[1]
[1]*University of Colorado, USA*
[2]*University of Washington, USA*

(Received 29 April 1998; revised 10 November 1998)

SUMMARY

Tomas and Webster note that in regions where there is a substantial cross-equator surface pressure gradient, there is locally anticyclonic absolute vorticity on the low pressure side of the equator and thus, the flow in this region meets the parcel criterion for inertial instability. They hypothesize that the atmospheric response to this absolute-vorticity distribution is a convergence–divergence doublet in the boundary layer. The convergence centre results in strong convection and thus is very important in determining the strength and location of convection (i.e. the intertropical convergence zones) whereas the divergence centre results in suppressed convection.

In this work, a zonally symmetric model of the boundary layer is developed to investigate this hypothesis further. An analysis of a linearized version of the model indicates that although the observed flow in these regions meets the parcel criterion for instability, it does not satisfy the linear stability criteria, because of the stabilizing influence of dissipation and the finite vertical scale. Much greater shear than that observed is required for linear instability. It is noted, however, that when the parcel criterion is met, one of the nonlinear terms which was neglected in the linear analysis may have an important influence on the flow.

Several experiments are performed integrating the full nonlinear model, relaxing back to a pressure distribution having a cross-equatorial gradient, to test whether the observed vorticity, wind and convergence distributions can be well simulated. It is found that the simulations reach a steady state in which there is a region of locally anticyclonic absolute vorticity on the low pressure side of the equator. This absolute-vorticity distribution results in an anomalous acceleration of the meridional wind and a convergence–divergence doublet, similar to that observed by Tomas and Webster. This response is explained as resulting from accelerations that act to bring the zonal flow out of geostrophic balance as it passes through the region of locally anticyclonic absolute vorticity. The response of the meridional wind to the strength of the pressure gradient is quasi-linear for small and somewhat larger values of forcing but, between these values, there is a range where the response is highly nonlinear, i.e. large increases in the strength of the meridional wind result from small changes in the pressure gradient. It is suggested that this nonlinear response may play a role in the observed sudden onset of the monsoon circulations.

The nonlinear model is also forced using pressure distributions taken from observations. The resulting steady-state simulated vorticity, wind and convergence distributions closely match the observations for the cases of pressure distributions taken from the east Pacific and east Atlantic during July. When forced using the pressure distribution from the Indian Ocean region during July, the model produces an unrealistically strong meridional wind response. Some improvement is obtained by including the latitudinally dependent zonal pressure gradient force, which is moderately strong in this region.

Finally, the model is forced using a pressure distribution taken from observations in the central Pacific Ocean during July. In this case the cross-equator pressure gradient is near zero. The simulated convergence is a maximum on the equator whereas observations show two convergence maxima that flank the equator; the observed convergence centres are associated with the convection that occurs in the region. Thus, the boundary layer dynamics as simulated by this model are not responsible for determining the location of convection in this region. It is suggested that in this case, the convection determines the boundary layer convergence, in contrast with the other cases, in which it is the boundary layer convergence that determines the convection.

KEYWORDS: Modelling Tropical dynamics

1. INTRODUCTION

In the past 25 years a number of hypotheses have been suggested to account for the observation that the intertropical convergence zone (ITCZ) is typically displaced some 4° to 12° from the equator and not necessarily collocated with the highest sea surface temperature (SST) and/or lowest sea-level pressure (SLP). As Waliser and Somerville (1994) and Tomas and Webster (1997) provide detailed reviews of these theories, they will only be mentioned briefly here. One of the first hypotheses to gain popularity was the idea that near the equator convection *should occur* over the regions of highest SSTs.

* Corresponding author: Program in Atmospheric and Ocean Sciences, University of Colorado, Campus Box 311, Boulder, CO 80309-0311, USA. e-mail: tomas@monsoon.colorado.edu

Pike (1971) found that in a coupled atmosphere–ocean model convection occurred over the SST maximum, which was displaced from the equator owing to upwelling which occurred at the equator in his zonally symmetric model. Manabe *et al.* (1974) provided support to the idea of the collocation of SST maxima and convection using an atmospheric general circulation model (GCM), but with specified climatological SSTs. Charney (1971) argued, on the other hand, that even if the SST is a maximum at the equator, convection will tend to occur away from the equator owing to the influence of conditional instability of the second kind (CISK). CISK depends on a cooperative feedback between boundary layer convergence and the internal heat source produced by the resulting convection. The boundary layer moisture convergence, upon which CISK depends, is a maximum away from the equator because the efficiency of boundary layer convergence increases with latitude. Holton *et al.* (1971) also invoked boundary layer convergence, but argued that the observed 4 to 5 day period westward propagating equatorial wave disturbances would have their maximum boundary layer convergence near the latitude where the Coriolis frequency equals the wave period, or about 6° latitude. This view received some support in a GCM study by Hess *et al.* (1993). Lindzen (1974), proposed a different mechanism whereby the low-level convergence field in near-equatorial convection results not from boundary layer processes, but from the dynamics of internal wave–CISK modes of equatorial disturbances. Waliser and Somerville (1994) provide some support for Charney's original notion, noting a positive feedback between boundary layer convergence and tropospheric heating by convection. Because of this feedback, it is argued that the maximum in convergence and convection is displaced from the equator, even when the SST maximum is on the equator.

The studies cited above appear to have sought a *general* explanation to account for the location of convection that is *independent* of the location within the tropics. Observational studies have suggested that considerable variation exists, not only in the longitude of the phenomena, but also in the relationship of convection to the underlying SST and local SLP minimum. Ramage (1974), Sadler (1975a,b), Hastenrath (1988) and Hastenrath and Lamb (1977a,b), among others, noted that the SST maximum and the low-level equatorial pressure trough often did not coincide with the location of organized convection (the ITCZ). Tomas and Webster (1997; hereafter referred to as TW) stratified the relationship between SST maxima, the local SLP minimum and the cross-equatorial pressure gradient. In regions where the surface cross-equatorial pressure gradient was weak, such as in the central Pacific Ocean, convection would tend to be collocated with the highest SSTs, which were in excess of 29 °C, and the lowest SLP. However, in regions where there existed a substantial cross-equatorial SLP gradient (e.g. the eastern Pacific, eastern Atlantic and North Indian Oceans during the boreal summer and the South Indian Ocean during the austral summer), organized convection occurred in the summer hemisphere, but equatorward of the SLP minimum and not necessarily collocated with the SST maximum. Furthermore, the outgoing long-wave radiation and divergent circulation fields indicated that, in spite of the fact that the SSTs were several degrees lower, convection was stronger in these regions compared to the central Pacific. TW attributed these observations to differences in the boundary layer dynamics, noting that in regions of strong cross-equatorial pressure gradient, the low-level convergence field associated with near-equatorial convection is closely associated with the displacement of the zero absolute-vorticity contour, $\eta = 0$, from the equator. In the space between the equator and the $\eta = 0$ contour they show that the flow satisfies the necessary condition for inertial instability given by the parcel method,

$$f\left(f - \frac{\partial \bar{u}}{\partial y}\right) < 0, \tag{1}$$

where f is the Coriolis parameter, $\bar{u}$ is the basic state zonal flow and y the meridional

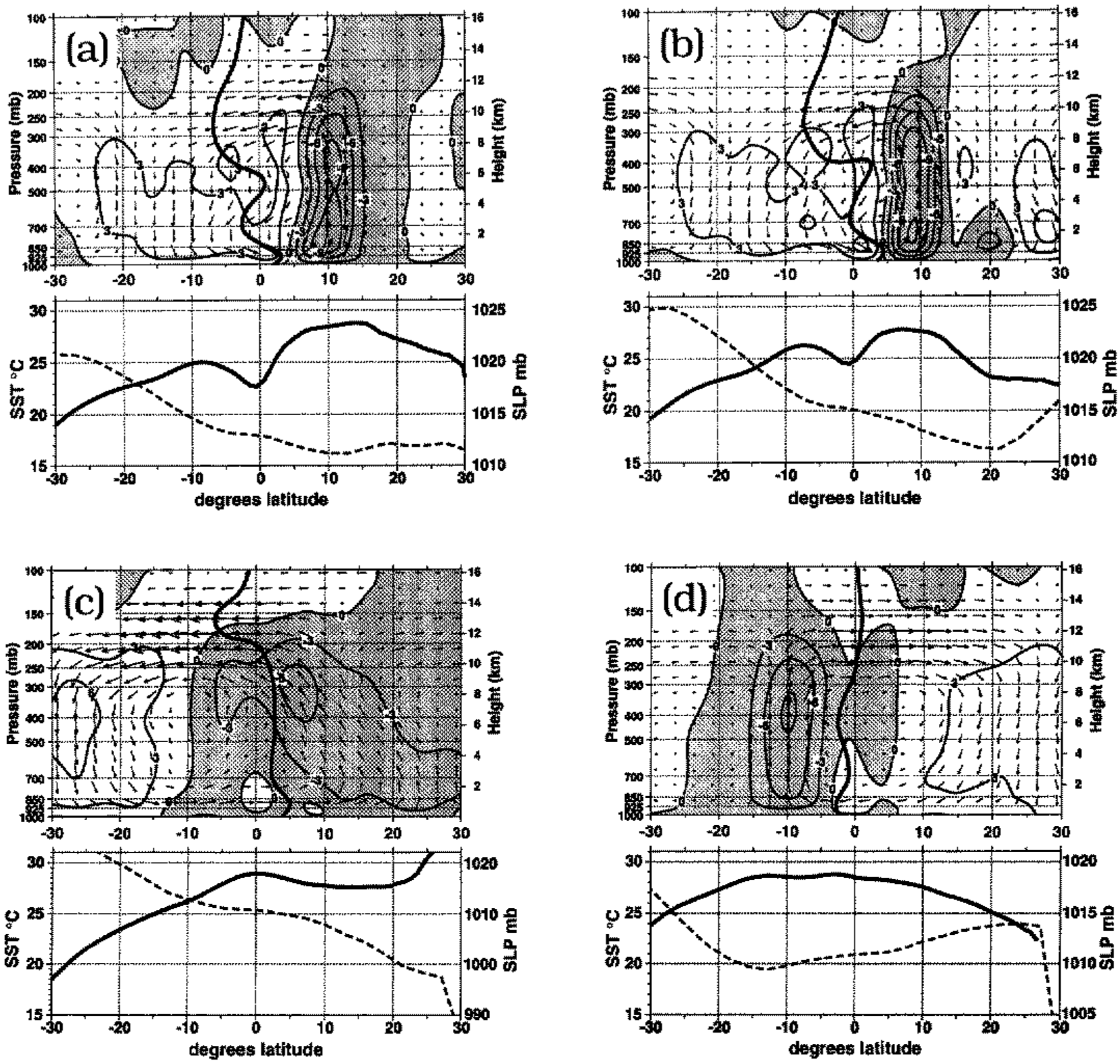

Figure 1. Latitude–height contours of the observed 1992–96 mean divergent circulation: (a) 120°W–90°E, (b) 30°W–0°, and (c) 55°E–85°E, all for July; (d) 55°E–85°W for February. Vertical velocity is in scaled pressure units $-50 \times$ mb s^{-1}($-50 \times \omega$), meridional velocity is in m s^{-1}; regions of rising motion are stippled and the zero absolute-vorticity contour ($\eta = 0$) is indicated in heavy black. Below each frame are sea-surface temperatures, (SST; solid line) in °C and sea-level pressures (SLP; dotted line) in mb.

distance. They argue that the meridional accelerations in the inertially unstable region account for the structure and the location of the near-equatorial low-level convergence, and thus, the strength and location of the ITCZ. Figure 1(a) to (d) shows the 1992–96 mean latitude–height cross-sections of divergent circulation in various months through four regions of the tropics where there exists a strong cross-equatorial surface pressure gradient. Regions of rising motion are stippled and the solid line shows the zero absolute-vorticity contour. In general, $\eta = 0$ is displaced from the equator into the summer hemisphere in the lower troposphere and into the winter hemisphere aloft. Maximum ascent (and convection) occurs on the poleward side of the $\eta = 0$ contour. Mean SST profiles for the same time period are shown below each panel.

The parcel method can only give a necessary condition for instability, since the influence of pressure perturbations on fluid accelerations is neglected. Indeed, analysis of the complete linear stability equations for the special case of constant zonal wind shear,

$\gamma \equiv \partial\bar{u}/\partial y$ (Dunkerton 1981; Stevens 1983), shows that only for inviscid flows with infinitesimal vertical-scale does (1) constitute a sufficient condition for instability. In the presence of dissipation, and/or for disturbances of finite vertical-scale, the zonal wind shear must exceed some critical value greater than f for unstable growth to occur.

In the cases examined by TW, displacement of the $\eta = 0$ line toward lower pressure occurs both in the planetary boundary layer and in the upper troposphere (Fig. 1). But the location of the convection is clearly associated with the $\eta = 0$ line in the boundary layer. In the atmospheric boundary layer over much of the equatorial ocean region, vertical mixing by buoyancy forces creates a mixed layer with depth of order 1 or 2 km on the time-scale of a few hours ($\approx 1 \times 10^4$ s). This is much shorter than the time-scale for meridional mixing by inertially unstable motions within a few degrees of the equator, which is comparable to an inertial period of several days ($\approx 4 \times 10^5$ s). Thus, a disturbance initiated by inertial instability in the equatorial boundary layer should be quickly mixed over the depth of the boundary layer, which is then the dominant vertical-scale for horizontal flow near the surface. Hence, (1) would not provide an accurate measure of linear inertial instability owing both to dissipation in the boundary layer, and to the finite vertical-scale of the horizontal flow in the mixed layer.

In section 2, we develop a simple slab model of the equatorial boundary layer that provides a basis for analysis of the role of inertial instability in the presence of a cross-equatorial pressure gradient. In section 3, we show by linear stability analysis that a much greater zonal wind shear than that suggested by the parcel criterion (1) would be required to produce linear inertial instability in the equatorial boundary layer.

The zonal wind shears, in the observations of TW are not strong enough to satisfy the linear inertial instability criteria. Although observed time-mean zonal flows in the regions where there is a substantial cross-equatorial pressure gradient in the lower troposphere are not inertially unstable in the conventional sense, the displacement of the $\eta = 0$ contour from the equator has a profound effect on the structure of the flow. In section 4 a nonlinear slab boundary layer model is used to demonstrate the influences of the $\eta = 0$ contour displacement across the equator. Examples of results using observed cross-equatorial surface pressure gradients are shown in section 5.

The general approach of the work undertaken in this study is to assume that the flow may be regarded as locally two-dimensional, and that the surface pressure distribution is determined by large-scale SST variability and land–sea distributions, which provide a fixed forcing for the near-equatorial flow.

The validity of the first assumption follows from the observations that show the flow in the regions of interest is primarily zonally symmetric, and that the divergent flow is dominated by the meridional component of the wind (TW, Figs. 2 and 9). This is supported further by comparing fields of $\partial u/\partial x$ and $\partial v/\partial y$ (not shown) with the total divergence. There tends to be some cancellation between the individual terms, however only the second term closely resembles the sum (the total divergence).

Some aspects of the validity of the second assumption, i.e. using the boundary layer approach for this study, will be discussed at the end of section 5.

2. The boundary layer model

Over a large part of the tropical oceans the planetary boundary layer is generally well mixed and extends to an altitude of approximately 1 or 2 km, where it is topped by a temperature inversion. A simple slab model for this type of tropical boundary layer was developed by Lindzen and Nigam (1987). A modified version by Battisti *et al.* (1999) forms the basis of the model developed here.

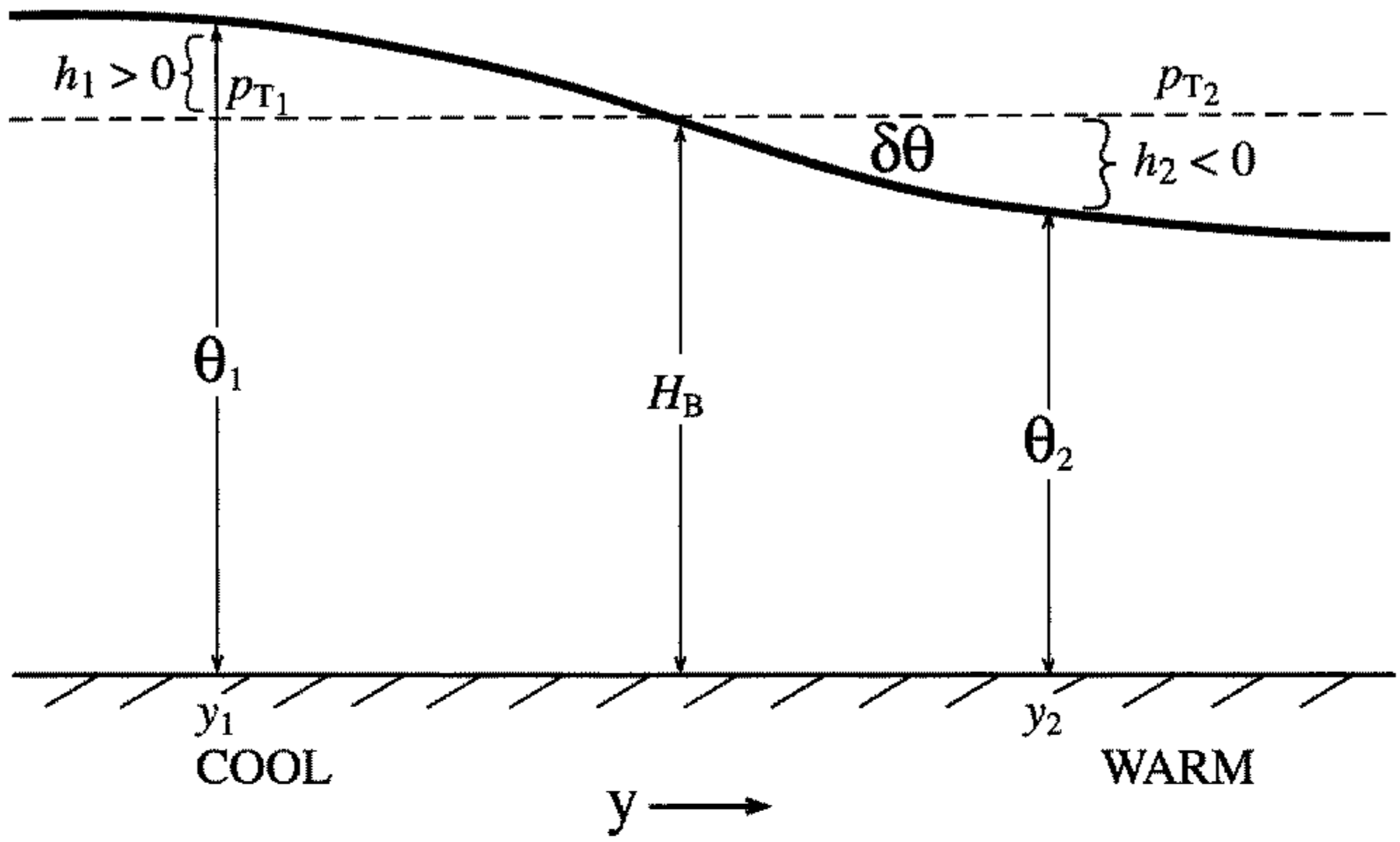

Figure 2. Schematic diagram illustrating the geometry of the boundary layer model. See text for explanation.

In the slab model, the boundary layer is assumed to be a well mixed slab with potential temperature, θ, and horizontal velocity, $\mathbf{V} = (u, v)$, which is assumed to be independent of height within the layer, and capped by a jump in potential temperature*, $\delta\theta$, at the top located at height $h_B(y, t)$. Also, the horizontal pressure gradient within the boundary layer is produced by the sum of the large-scale pressure gradient at the boundary layer top and the pressure gradient owing to the meridional temperature gradient within the boundary layer. The meridional temperature gradient is closely related to the SST and the land–sea distribution. In the derivation that follows, zonal symmetry is assumed.

The potential temperature in the boundary layer is given by $\theta_B(y) = \theta_0 + \theta(y)$, where θ_0 is a reference state potential temperature and $\theta(y)$ is the meridionally dependent deviation from θ_0, as determined from the large-scale surface temperature field. Similarly, the density in the boundary layer is given by, $\rho_B = \rho_0 + \rho(y, z)$; where ρ_0 is the reference state (constant) density and $\rho(y, z)$ varies both meridionally and with height. Letting H_B be the mean boundary layer depth and $h(y)$ the departure from H_B at any latitude, allows us to specify the height of the boundary layer as, $h_B = H_B + h(y)$.

Figure 2 shows the geometry of the model used for computing the mid-level pressure distribution in the boundary layer. The pressure at level $z = H_B$ for a constant depth boundary layer ($h = 0$) is given by P_T. Then, for example, the pressure at level z in the boundary layer for columns at y_1 (where $h > 0$) and y_2 (where $h < 0$) can be computed by integrating downward for $z = H_B$ provided that the pressure in column 1 is corrected to reflect the fact that, because $h_1 > 0$, the total pressure at $z = H_B$ in column 1 will be greater than the free-atmosphere value P_{T1}, since between the levels H_B and $H_B + h$ the free-atmosphere air is replaced by denser boundary layer air. Thus,

$$P(y_1, z) = P_{T1} - \int_{H_B}^{H_B+h_1} \delta\rho g \, dz + \int_z^{H_B} (\rho_0 + \rho_1) g \, dz,$$

* Lindzen and Nigam (1987) and Battisti *et al.* (1998) use the virtual potential temperature in their formulations, thus accounting for small differences in density owing to differences in the water vapour content. Given other approximations in our model formulation, we feel that this is probably unwarranted.

$$P(y_2, z) = P_{T2} + \int_{H_B+h_2}^{H_B} \delta\rho g \, dz + \int_z^{H_B} (\rho_0 + \rho_2) g \, dz.$$

where g is the acceleration due to gravity. Letting $z = H_B/2$ and integrating yields

$$P(y_2, H_B/2) - P(y_1, H_B/2) = (P_{T2} - P_{T1}) - \delta\rho g(h_2 - h_1) + (\rho_2 - \rho_1)\frac{gH_B}{2}. \quad (2)$$

We now assume that $|\theta| \ll \theta_0$, $|\rho| \ll \rho_0$, and $|\delta\theta| \ll \theta_0$ so that

$$\frac{\rho}{\rho_0} \approx -\frac{\theta}{\theta_0} \quad \text{and} \quad \frac{\delta\rho}{\rho_0} \approx -\frac{\delta\theta}{\theta_0},$$

(e.g. Holton 1992).

Defining $g' = g\delta\theta/\theta_0$ and $\Gamma = gH_B/(2\theta_0)$, substituting into (2), dividing by $\rho_0(y_2 - y_1)$ and taking the limit $y_2 - y_1 \to 0$ gives

$$\frac{\partial\Phi}{\partial y} \equiv \frac{1}{\rho_0}\frac{\partial P}{\partial y} = \frac{1}{\rho_0}\frac{\partial P_T}{\partial y} + g'\frac{\partial h}{\partial y} - \Gamma\frac{\partial\theta}{\partial y}. \quad (3)$$

This expression shows that the pressure gradient in the boundary layer depends on P_T, h and θ.

For the basic state for the linearized model ($\bar{u}$), and the initial state for the nonlinear model (Φ), it is convenient to assume that $h = 0$ and that the pressure field is in geostrophic balance with a basic state zonal wind, $\beta y\bar{u} = -\partial\bar{\Phi}/\partial y$ (by assuming that $h = 0$ we are choosing to specify the basic state in terms of $\partial\bar{\Phi}/\partial y$ rather than $\partial h/\partial y$). But from (3) the basic state then must satisfy

$$\frac{\partial\bar{\Phi}}{\partial y} = \frac{1}{\rho_0}\frac{\partial P_T}{\partial y} - \Gamma\frac{\partial\bar{\theta}}{\partial y}. \quad (4)$$

If $\bar{\theta}(y)$ is assumed to be given by a specified surface temperature distribution, then it is necessary to specify P_T/ρ_0 so that (4) yields a $\bar{\Phi}(y)$ field that geostrophically balances the basic state wind.

To determine Φ in (3), we need an equation governing the variable boundary layer height, h. Vertical integration of the continuity equation gives

$$\int_0^{H_B} \left(\frac{\partial v}{\partial y}\right) dz + w(h_B) = -\epsilon h$$

where, following Battisti *et al.* (1999), the right-hand side assumes that small-scale processes relax the boundary layer depth toward its mean value on a time-scale ϵ^{-1}. In section 5, we discuss how the value of epsilon can be varied to incorporate the effect of convection upon the stability. The vertical velocity at the top of the boundary layer is given by

$$w(h_B) = \frac{Dh_B}{Dt} = \frac{Dh}{Dt} = \frac{\partial h}{\partial t} + v\frac{\partial h}{\partial y},$$

so that

$$g'\left(\frac{\partial h}{\partial t} + v\frac{\partial h}{\partial y}\right) + C_B^2\frac{\partial v}{\partial y} = -\epsilon(g'h), \quad (5)$$

where $C_B^2 \equiv g' H_B$. Now, from (3) and (4), $g'h = \Phi - \bar{\Phi} + \Gamma(\theta - \bar{\theta})$. For simplicity we assume that the potential temperature in the boundary layer instantaneously adjusts to the surface temperature, θ_{ST}, so that

$$g'h = \Phi - \bar{\Phi}. \tag{6}$$

The complete model now becomes

$$\frac{\partial u}{\partial t} + v\left(\frac{\partial u}{\partial y} - \beta y\right) + \alpha u = 0, \tag{7}$$

$$\frac{\partial v}{\partial t} + v\frac{\partial v}{\partial y} + \beta y u + \frac{\partial \Phi}{\partial y} + \alpha v = 0, \tag{8}$$

$$\frac{\partial \Phi}{\partial t} + v\frac{\partial}{\partial y}(\Phi - \bar{\Phi}) + C_B^2\frac{\partial v}{\partial y} = -\epsilon(\Phi - \bar{\Phi}), \tag{9}$$

which, linearized about the basic state $\bar{u}$, becomes

$$\frac{\partial u'}{\partial t} + v'\left(\frac{\partial \bar{u}}{\partial y} - \beta y\right) + \alpha u' = 0, \tag{10}$$

$$\frac{\partial v'}{\partial t} + \beta y u' + \frac{\partial \Phi'}{\partial y} + \alpha v' = 0, \tag{11}$$

$$\frac{\partial \Phi'}{\partial t} + C_B^2\frac{\partial v'}{\partial y} = -\epsilon \Phi', \tag{12}$$

where α is the linear momentum damping coefficient. Note that (6)–(9) and (10)–(12) describe the flow at $z = H_B/2$ whereas (linearized) equations (6) and (11) in Battisti *et al.* (1999) describe the vertically averaged flow in the boundary layer. The two sets of linearized equations are similar except that those presented here retain time dependence and the horizontal advection of momentum.

3. Linearized inertial stability model

As shown by Dunkerton (1981) an analytical solution to (10)–(12) can be obtained in the case of constant mean shear

$$\bar{u} = \gamma y, \tag{13}$$

where γ is the proportionality constant relating the zonal flow to the meridional distance. Eliminating u' and Φ' from (10)–(12) gives

$$\left(\frac{\partial}{\partial t} + \alpha\right)^2 v' + \{\beta y(\beta y - \gamma)\}v' - C_B^2\frac{\partial^2 v'}{\partial y^2} = 0, \tag{14}$$

which has solutions of the form $v'(y, t) = V(y)e^{i\omega t}$, where $V(y)$ satisfies

$$\frac{\partial^2 V}{\partial y^2} - \frac{1}{C_B^2}\{\beta y(\beta y - \gamma) - (\omega - i\alpha)^2\}V = 0. \tag{15}$$

In order to simplify the mathematics, it has been assumed that $\epsilon = \alpha$. Although the two constants are associated with different processes, it is reasonable to expect them to have similar magnitude. Equation (15) can be put into standard form by shifting coordinates

$$y' \equiv y - \frac{\gamma}{2\beta};\ \omega'^2 \equiv (\omega - i\alpha)^2 + \frac{\gamma^2}{4}.$$

We now define a non-dimensional coordinate $\nu \equiv (\beta/C_B)^{\frac{1}{2}} y'$ and transform (15) to become

$$\frac{d^2 V}{d\nu^2} + \left(\frac{\omega'^2}{\beta C_B} - \nu^2\right) V = 0. \tag{16}$$

Equation (16) has solutions with $V(\nu) \to 0$ and $\nu \to \pm\infty$ provided that $\omega'^2/(\beta C_B) = 2n+1, n = 0, 1, 2, \ldots$.

For $n = 0$, the solution has the form

$$V(\nu) = V_0 \exp\left(\frac{-\nu^2}{2}\right). \tag{17}$$

In this case the eigenvalue is given by

$$\omega'^2 = \beta C_B = (\omega - i\alpha)^2 + \frac{\gamma^2}{4}. \tag{18}$$

Equation (18) shows that instability (i.e. ω is imaginary) only occurs for γ greater than a critical value. Only if $\alpha \to 0$ and $C_B \to 0$ will instability occur for $\gamma \to 0$. In the inviscid case $\gamma^2 > 4\beta C_B$ for instability, so that the flow is neutrally stable if $\gamma^2 = 4\beta C_B$. If we assume that the potential-temperature jump at the boundary layer top is about 3 K and the boundary layer depth is 1 km, then $C_B = (gH_B\delta\theta/\theta_0)^{1/2} \simeq 10$ m s^{-1}. But then instability requires that $\gamma \geqslant 3 \times 10^{-5}$ s^{-1} so that the flow speed must increase by 30 m s^{-1} over 10° of latitude,just for neutrality. Including boundary layer dissipation by letting $\alpha = 0.5 \times 10^{-5}$ s^{-1} (i.e. ~ 2 day damping time) raises the critical shear for instability to $\gamma > 3.2 \times 10^{-5}$ s^{-1}. This is a much larger shear than the observed zonal wind shear of TW, and we conclude that the observed state does not satisfy the linear instability criteria (it is worth noting the weak dependence of critical shear on inversion strength, in that $\gamma \sim \delta\theta^{1/4}$, making the linear result robust). Nevertheless, the proximity of the zero absolute-vorticity line and the off-equator convection suggests that the dynamics inherent in (1) play a significant role in determining the location of convection.

4. Nonlinear solutions for an idealized cross-equatorial pressure gradient

Examination of the zonal momentum equation, (7), indicates that the sign of the meridional advection term will be reversed in regions in which the criterion (1) is satisfied. This sign reversal suggests that nonlinear dynamics associated with regions of anomalous anticyclonic absolute vorticity may be important in the equatorial boundary layer. To examine this possibility we solve (7)–(9) with a specified large-scale basic pressure field and examine the response of the boundary layer to the imposed forcing.

Consider a steady-state basic state pressure given by

$$\bar{\Phi}(y) = -\beta u_0 \left\{\left(\frac{D}{\pi}\right)^2 \sin\left(\frac{\pi y}{D}\right) - \left(\frac{Dy}{\pi}\right)\cos\left(\frac{\pi y}{D}\right)\right\}, \tag{19}$$

where D is the domain half-width, then

$$\frac{\partial \bar{\Phi}}{\partial y} = -\beta u_0 y \sin\left(\frac{\pi y}{D}\right),$$

and the geostrophic wind is given by

$$\overline{u_g(y)} = u_0 \sin\left(\frac{\pi y}{D}\right).$$

In this basic state, $\eta = 0$ at y_c, satisfying $\beta y_c = (\pi u_0/D)\cos(\pi y_c/D)$. Observations suggest choosing $u_0 = 10$ m s^{-1} and $D = 3 \times 10^6$ m, resulting in the zero absolute-vorticity contour being located at $y_c \simeq 400$ km or at approximately 4° latitude.

The dissipation terms in (7) and (8) represent the slab boundary layer surface stress (e.g. Young 1988), which depends strongly on the surface wind speed. An appropriate model is the bulk aerodynamic formulation in which we let

$$\alpha = \frac{C_D}{H_B}|\mathbf{V}| = 0.5 \times 10^{-6}|\mathbf{V}|,$$

where C_D is the drag coefficient. This value implies a 2-day damping time for $|\mathbf{V}| = 10$ m s^{-1}, which is reasonable. Integrations using larger values of α (by a factor of 2 to 3) resulted in meridional wind maxima that had decreased amplitude and were broader in latitudinal extent. In general, larger values of α reduced the extent and influence of the locally anticyclonic absolute vorticity in the solutions.

Following Battisti *et al.* (1999) we assume that the boundary layer is ventilated on a time-scale of about one day so that $\epsilon = 1.0 \times 10^{-5}$ s^{-1}, and we again set $C_B^2 = 100$ m^2 s^{-2} in (9).

In order to evaluate the role of the anomalous zonal acceleration in (7) caused by an off-equator location of the $\eta = 0$ contour, we compare the steady-state solutions for (7)–(9), Case 1, with solutions for the same conditions except that $v(\beta y - \partial u/\partial y)$ is replaced by $\beta y v$ in (7), Case 2. That is to say, in Case 2 the (nonlinear) advection of the zonal wind is neglected.

Figure 3 shows the results of the calculations. In Case 1 the zero absolute-vorticity contour is shifted to about 6°N and is nearly coincident with a sharp maximum in v. As a result there is strong convergence poleward of the $\eta = 0$ line and divergence equatorward. By contrast, in Case 2, in which only the $\beta y v$ term is included, the meridional wind has a much broader and weaker profile with only weak convergence well poleward of that in Case 1. Note that if only the linear part of the advection of the zonal wind is included, $v'\partial\overline{u_g(y)}/\partial y$, the results are similar to those for Case 2.

The effect that the divergence has upon the mass distribution can be seen in Fig. 3(f) which shows the difference between the simulated geopotential and the basic state. Not surprisingly, the two quantities show a high degree of negative correlation and this part of the mass field acts to oppose the meridional flow.

We conclude that the anomalous acceleration in the region of $\eta < 0$ in the northern hemisphere provides strong amplification of the boundary layer meridional circulation, thus leading to convergence and convection just poleward of the $\eta = 0$ line. The amplification occurs because the meridional flow through the region of locally anticyclonic absolute vorticity tends to bring the zonal flow out of geostrophic balance, requiring a local meridional wind maximum to maintain balance in the steady-state equations. This can be seen by rewriting the steady-state version of (7) and (8) as

$$-v\left(\beta y - \frac{\partial u}{\partial y}\right) + \alpha u = 0, \tag{20}$$

$$+v\frac{\partial v}{\partial y} + \beta y u + \frac{\partial \Phi}{\partial y} + \alpha v = +v\left(\frac{\partial v}{\partial y} + \alpha\right) + \beta y u_{ag} = 0, \tag{21}$$

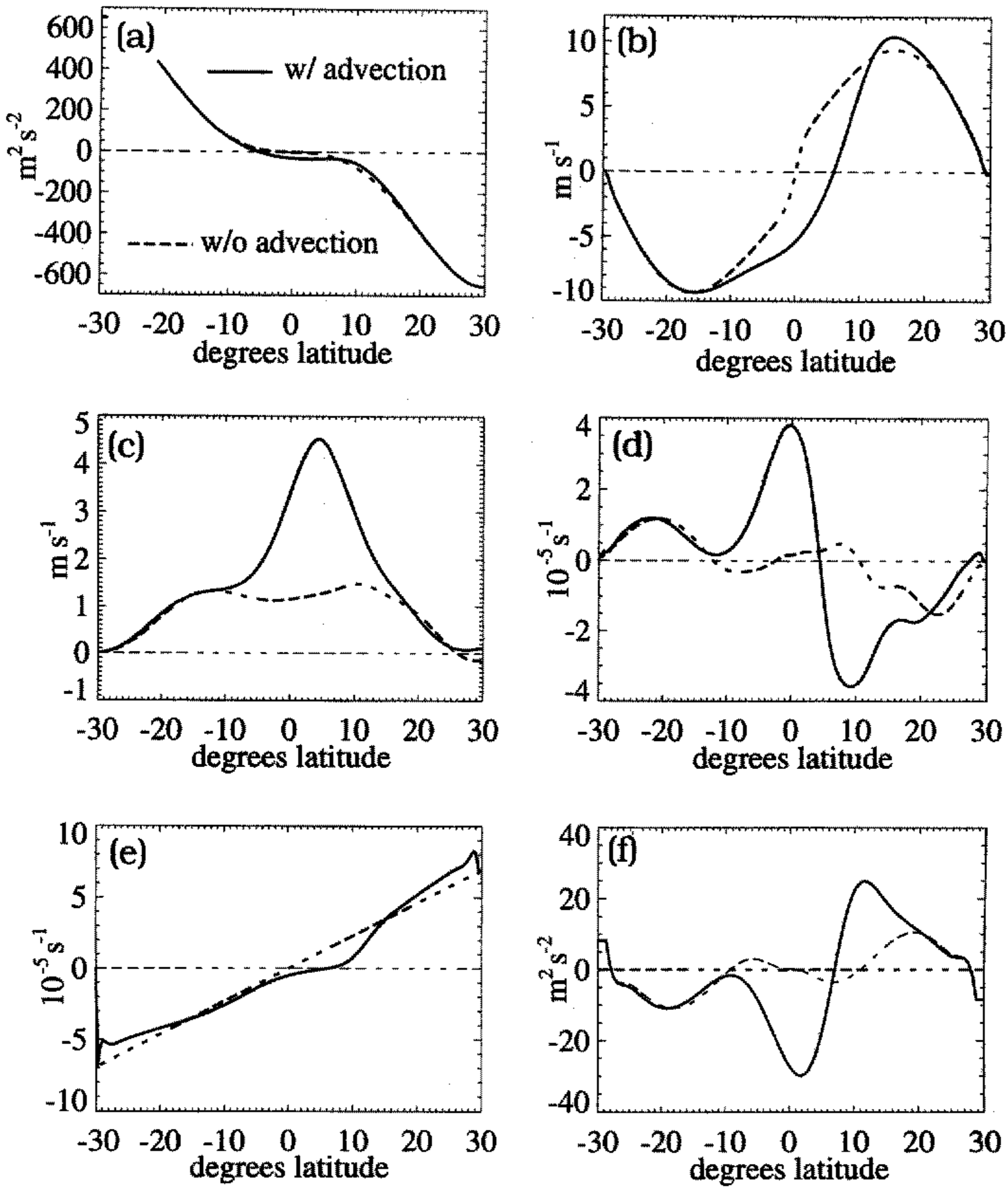

Figure 3. Latitudinal profiles of simulated steady-state parameters obtained using the idealized forcing: (a) geopotential (m^2s^{-2}), (b) zonal wind ($m\ s^{-1}$), (c) meridional wind ($m\ s^{-1}$), (d) divergence ($10^{-6}\ s^{-1}$), (e) absolute vorticity ($10^{-5}\ s^{-1}$) and (f) difference between the simulated and basic state geopotential ($m^2\ s^{-2}$). Solid lines indicate the case with the term $v\partial u/\partial y$ (see text) included; dashed lines indicate the case with the term omitted.

where

$$u_{ag} = u + 1/(\beta y)\partial\Phi/\partial y$$

is the zonal ageostrophic wind. Northward cross-isobaric flow occurs at low latitudes where the pressure gradient force is directed northward, the Coriolis parameter is small and dissipation is non-zero. This northward flow appears in (20) where it multiplies the absolute vorticity. For the steady-state solution to exist, the advection of absolute vorticity

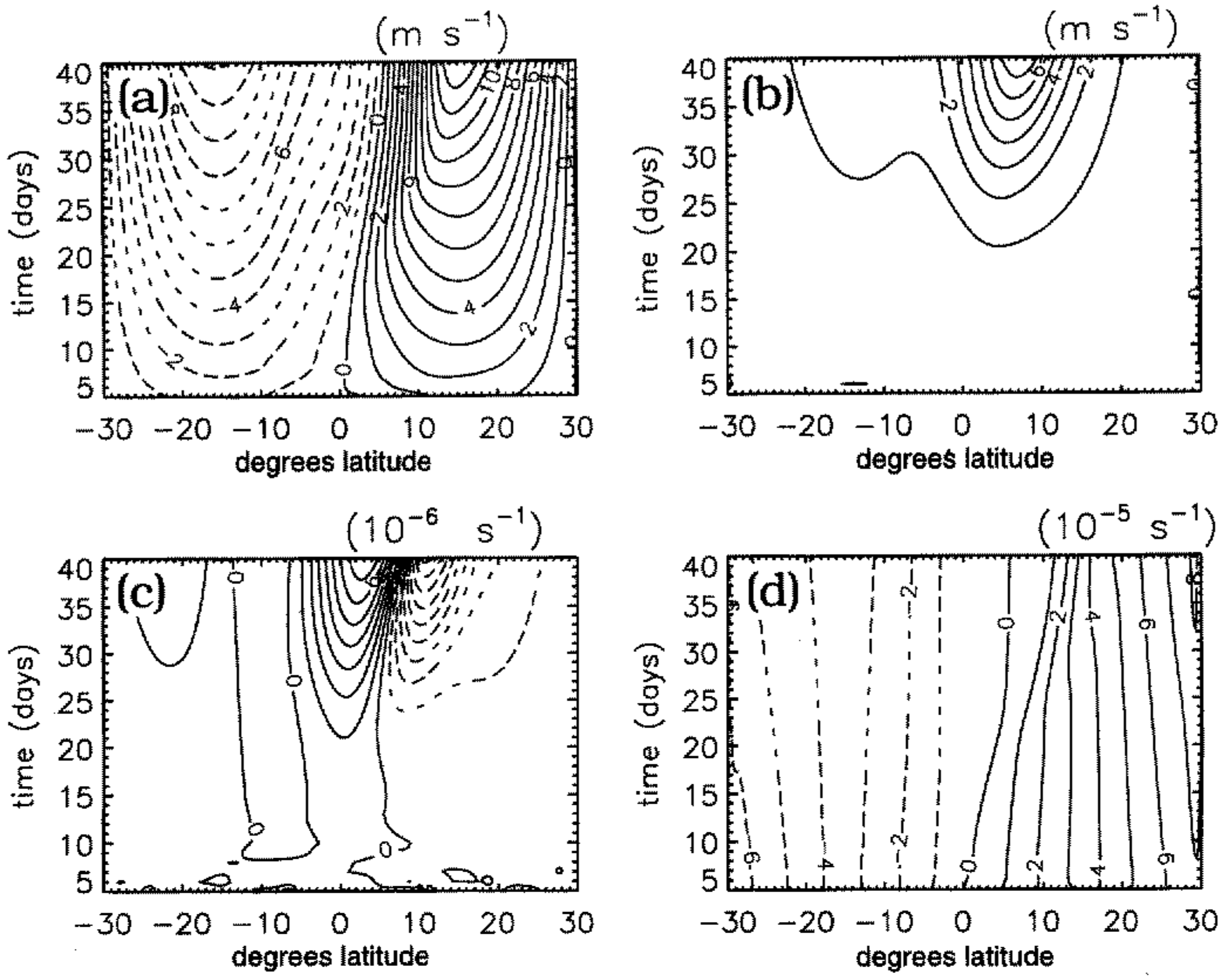

Figure 4. Latitude–time contours of the simulated time dependent parameters obtained using the idealized forcing with amplitude increasing linearly with time: (a) zonal wind (m s^{-1}), (b) meridional wind (m s^{-1}), (c) divergence (10^{-6} s^{-1}), and (d) absolute vorticity (10^{-5} s^{-1}).

must be balanced by dissipation of the zonal flow. Thus there must be westerlies where the absolute vorticity is positive and easterlies where the absolute vorticity is negative. Because of the northward directed pressure gradient force, the easterlies which lie to the north of the equator and south of the $\eta = 0$ contour, cannot be in geostrophic balance. The easterly ageostrophic flow appears in (21), requiring northward flow for balance when $(\partial v/\partial y + \alpha) > 0$. At the location of the maximum in the meridional divergent wind ($\mathrm{d}v/\mathrm{d}y = 0$), frictional dissipation balances the acceleration owing to the Coriolis parameter multiplying the ageostrophic zonal flow.

Because of the nonlinearity in (7)–(9), the amplitude of the boundary layer convergence need not vary linearly with the magnitude of the basic state cross-equatorial pressure gradient. It is useful to examine how large this pressure gradient must be in order to force a significant off-equator convergence response. The dependence of the solution on the forcing was tested by solving the system (7)–(9) for an idealized forcing with the same analytic form as (19), but with amplitude increasing linearly from zero up to the steady-state value used for the solutions of Fig. 3 over a 40-day period. Note that the rate at which the forcing is increased is sufficiently slow, compared to the rate at which steady state is approached, for the model to be very close to steady state during the entire time the forcing is changed. Contour plots of the time-dependent solution fields are shown in Fig. 4. The easterly and westerly zonal wind maxima (Fig. 4(a)) increase approximately linearly with the increasing pressure gradient forcing, and the zero wind contour is grad-

ually displaced into the northern hemisphere by meridional advection. The displacement of the zero contour of absolute vorticity from the equator increases approximately linearly with time until it reaches about 4 degrees of latitude by day 20; thereafter it increases only slowly to a maximum of about 5 degrees (Fig. 4(b)). The cross-isobaric meridional wind and accompanying divergence field (Fig. 4(c) and (d)) remain very weak until after day 20, and then increase very rapidly with further increases in the forcing. Consistent with the observational findings of TW, the meridional wind is a maximum near the zero absolute-vorticity contour and there is strong convergence poleward of the zero absolute-vorticity contour.

The nonlinear behaviour of the meridional wind and divergence fields suggest that a critical amplitude of the cross-equatorial pressure difference must be exceeded in order to drive a strong meridional flow and create strong convergence. This behaviour in the simple idealized model suggests that one explanation for the sudden onset of observed monsoon circulations may be the development of cross-equatorial pressure difference exceeding such a critical value.

5. Solution for observed pressure fields

Observed pressure distributions are, of course, more complex than the idealized field expressed in (19). Forcing the model using observed geopotential distributions and comparing the simulated flow with observations is an important test of the model. If the model produces reasonable agreement with observations, it is likely that it includes the essential physical processes that determine the characteristics of the flow. Poor agreement with the observations would indicate that an important process (or perhaps more than one) is missing. An analysis of the discrepancies may then provide valuable clues that help identify the missing process(es).

As stated in the introduction, TW noted that there are several regions where there exists a strong low-level, cross-equatorial pressure gradient and where the $\eta = 0$ contour is displaced several degrees from the equator. Associated with these features, there is a meridional divergent wind maximum and a divergence/convergence doublet. Examples of these locations were shown in Fig. 1. Guided by these observations, we performed experiments in which the model was forced using observed data, zonally averaged over longitude bands representative of the following three regions; 120°W to 90°W for the east Pacific, 30°W to 10°W for the Atlantic and 60°E to 80°E for Indian Ocean. An additional case was run for the Indian Ocean in which the latitudinally dependent zonal pressure gradient force was included in (7). A control case, in which the model was forced using a geopotential distribution that is nearly flat across the equator representative of the central Pacific between 165°E to 165°W, is also examined. In Figs. 5–9, panels (a) show the geopotential, (b) the zonal wind, (c) the meridional wind, (d) the divergence and (e) the absolute vorticity. Simulations are plotted using dashed lines and observations as heavy black lines.

For convenience, we use the observed 925 mb geopotential in these experiments, assuming that the geopotential is determined by the underlying SSTs and pressure at the top of the boundary layer as specified by (3). The data source is the European Centre for Medium-Range Weather Forecasting (ECMWF) operational analyses, made available by the National Center for Atmospheric Research (NCAR). Harris and Vecchi (1997) have addressed the issue of the accuracy of the divergent component of these analyses by:

(i) Comparing the climatological 10 m winds and divergence calculated from the ECMWF operational analyses with the same quantities calculated from the Comprehensive Ocean–Atmosphere DataSet;

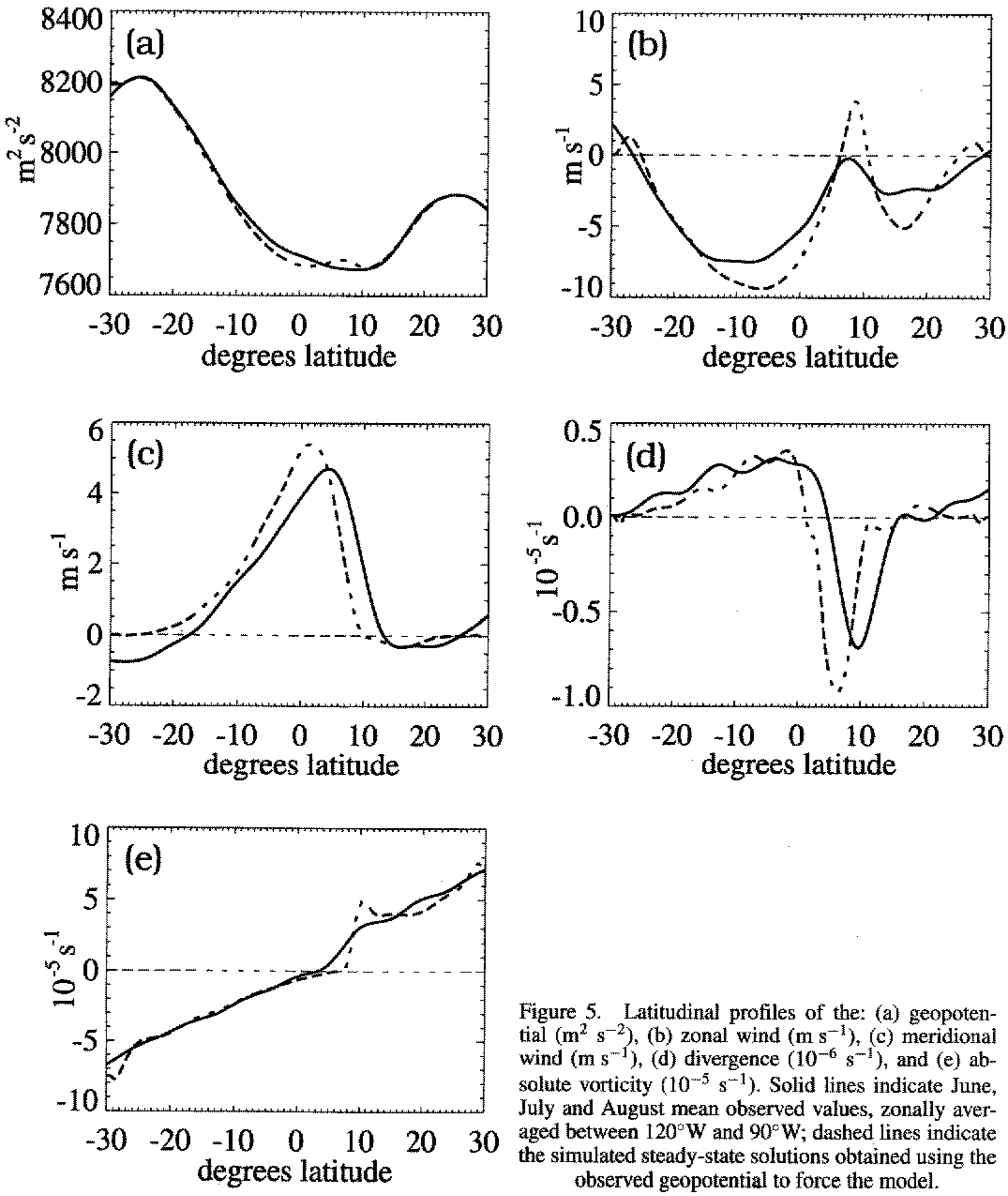

Figure 5. Latitudinal profiles of the: (a) geopotential ($m^2\ s^{-2}$), (b) zonal wind ($m\ s^{-1}$), (c) meridional wind ($m\ s^{-1}$), (d) divergence ($10^{-6}\ s^{-1}$), and (e) absolute vorticity ($10^{-5}\ s^{-1}$). Solid lines indicate June, July and August mean observed values, zonally averaged between 120°W and 90°W; dashed lines indicate the simulated steady-state solutions obtained using the observed geopotential to force the model.

(ii) Calculating the root mean square (r.m.s.) difference between the 10 m winds from the ECMWF operational analyses and available data from the Tropical Ocean Global Atmosphere (TOGA) Tropical Atmosphere Ocean (TAO) array.

Their results show a high degree of agreement between the various datasets. In addition, we have looked at the National Center for Environmental Prediction (NCEP) reanalyses and found that although the magnitude of the divergent flow is weaker in the NCEP analyses, there is general agreement in the location of key features such as the $\eta = 0$ contour and the divergent wind maxima in the regions of interest.

For all these cases, it is assumed that convection occurs when there is moderately strong convergence within the boundary layer, and the boundary layer experiences in-

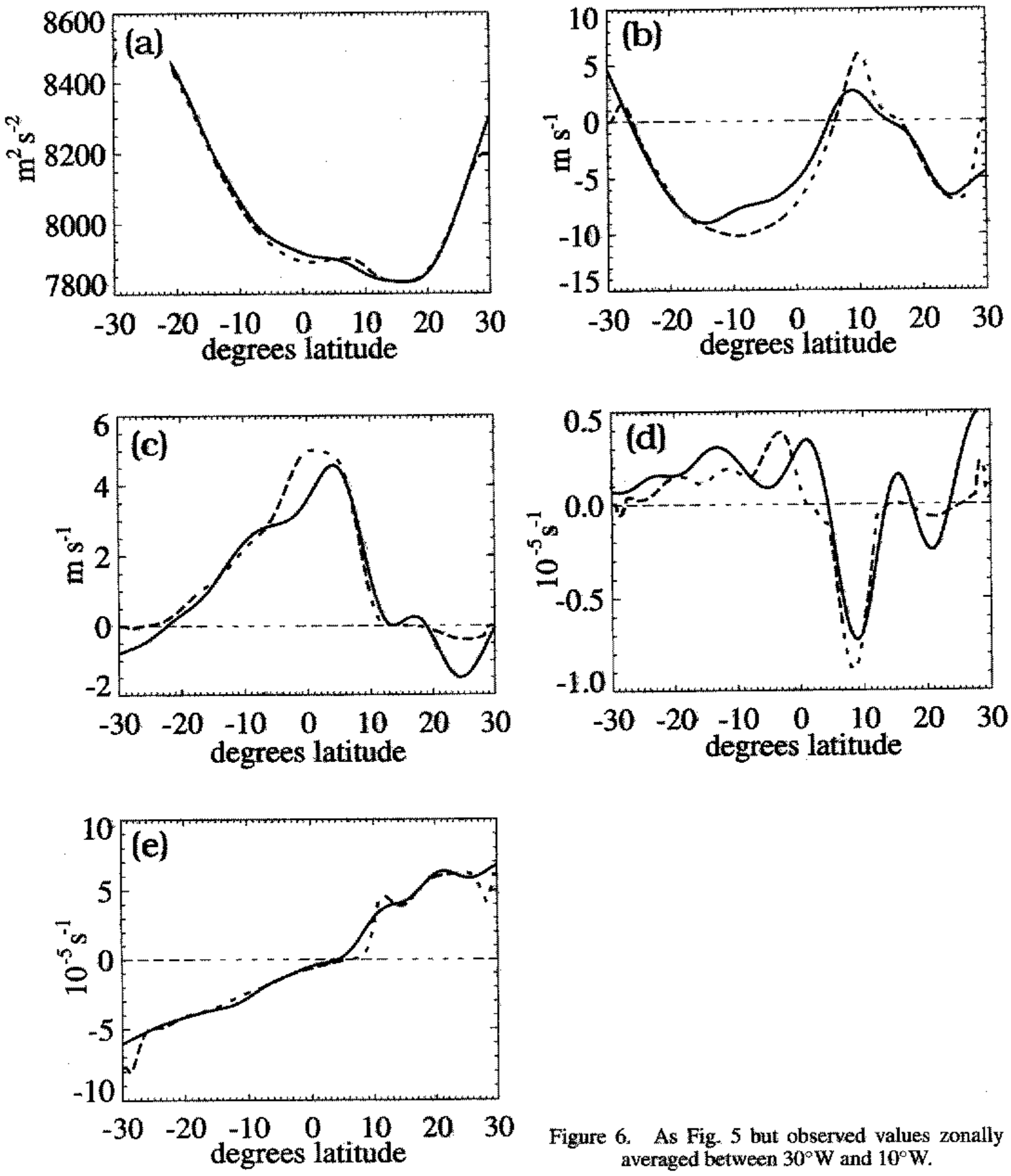

Figure 6. As Fig. 5 but observed values zonally averaged between 30°W and 10°W.

creased venting as a result of the convection (Battisti *et al.* 1999). This process was parametrized by decreasing the relaxation time ($1/\epsilon$) by a factor of 3 when the convergence exceeded values greater than 2×10^{-6} s^{-1}. Note that the factor of 3 for convective relaxation gives roughly an 8-hour time-scale, consistent with Battisti *et al.* (1999). The value of this factor was chosen to provide reasonable agreement between the simulations and the observations. Using larger values resulted in meridional wind maxima that were stronger and located slightly further from the equator than those in observations; smaller values had the opposite effect. This response is a result of the geopotential distribution being influenced by the mass divergence and convergence associated with the meridional wind maximum. The divergence/convergence doublet acts to lower geopotential to the south of the wind maximum and raise it to the north, and thus attempts to produce a local

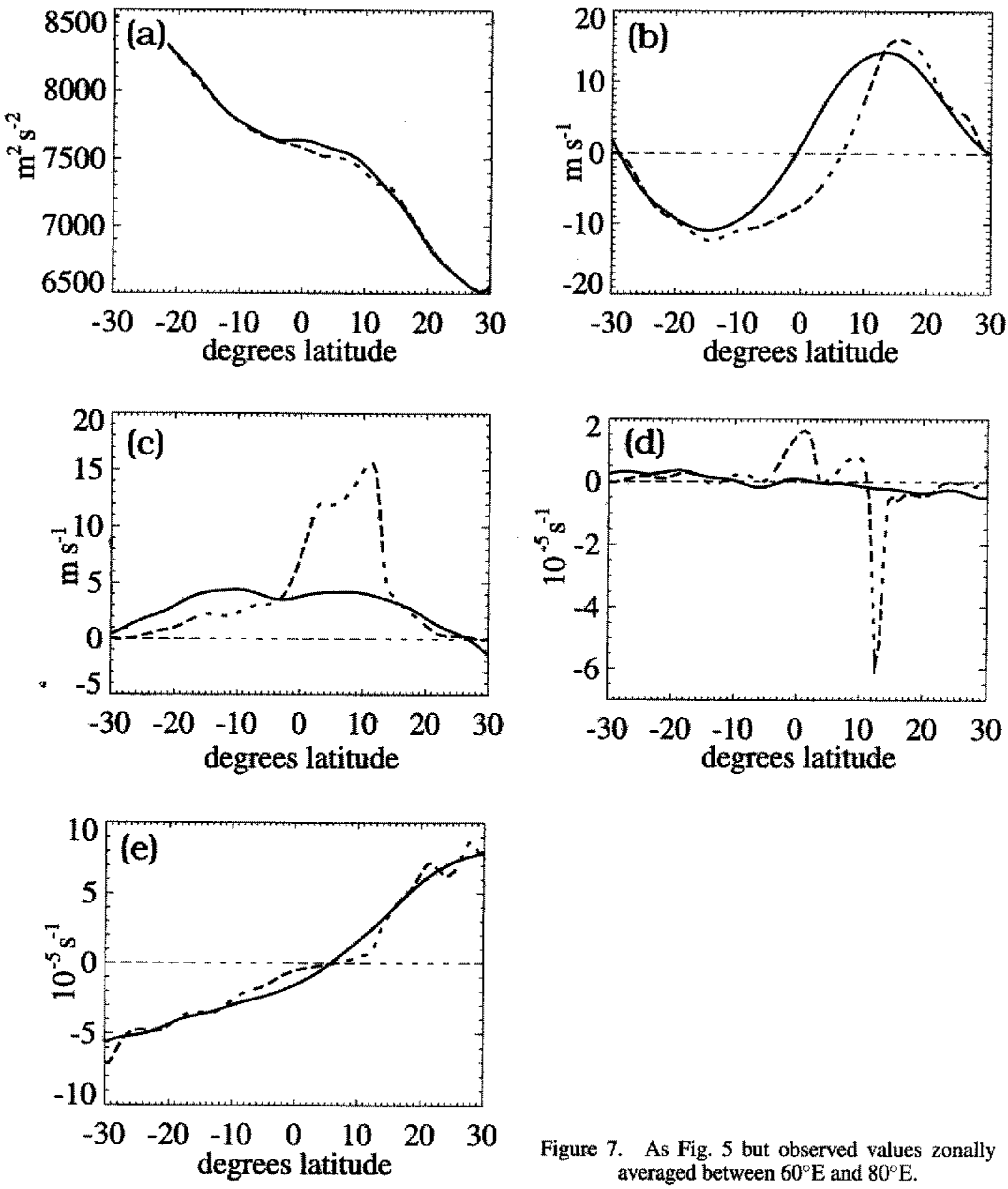

Figure 7. As Fig. 5 but observed values zonally averaged between 60°E and 80°E.

geopotential gradient in opposition to the large-scale geopotential gradient. This effect can be seen in the simulated, but not the observed, geopotential distributions for the east Pacific and Atlantic cases (Figs. 5(a) and 6(a)). Note that had the factor multiplying $1/\epsilon$ been reduced or omitted, this feature would attain greater amplitude than is seen in these figures. The model was found to be fairly insensitive to the value of the convergence threshold used, as long as it was somewhat less than the maximum convergence simulated by the model ($\approx 5 \times 10^{-6}$ s^{-1}). We applied this venting formulation to the idealized case and found that it resulted in an increase in the amplitude of the meridional wind maximum of approximately 1.5 m s^{-1} and shifted it northward several degrees of latitude.

The results for the east Pacific and Atlantic cases are very similar and therefore will be discussed collectively. Both cases show good agreement between the simulations and

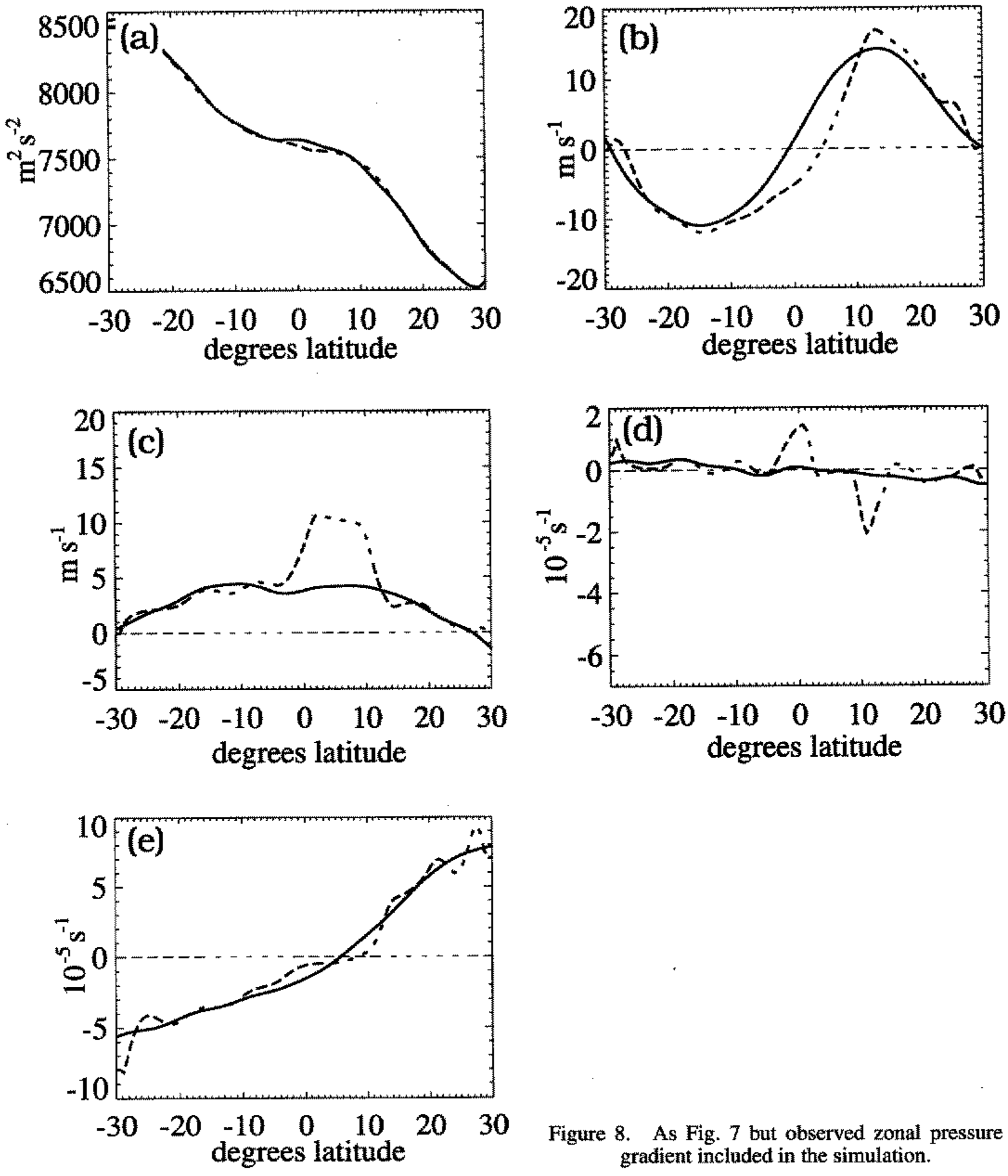

Figure 8. As Fig. 7 but observed zonal pressure gradient included in the simulation.

the observations. Key features simulated by the model and also seen in the observations include a large region of easterlies in the southern hemisphere with a broad maximum (minimum in zonal wind speed) located between 5°S and 15°S (Figs. 5(b) and 6(b)). The easterlies extend across the equator and several degrees into the northern hemisphere. As we showed in section 3, these easterlies in the northern hemisphere, in conjunction with the northward directed pressure gradient force, are crucial for the existence of the local meridional wind maximum. Westerlies are found to the north of the easterlies, but in the simulations they are too strong and located slightly too far north (this impacts the simulated absolute-vorticity distribution leading to discrepancies there as well, as discussed below). The model simulates the northward wind maximum located just off the equator very well (Figs. 5(c) and 6(c)); a small discrepancy occurs in the east Pacific where the simulated

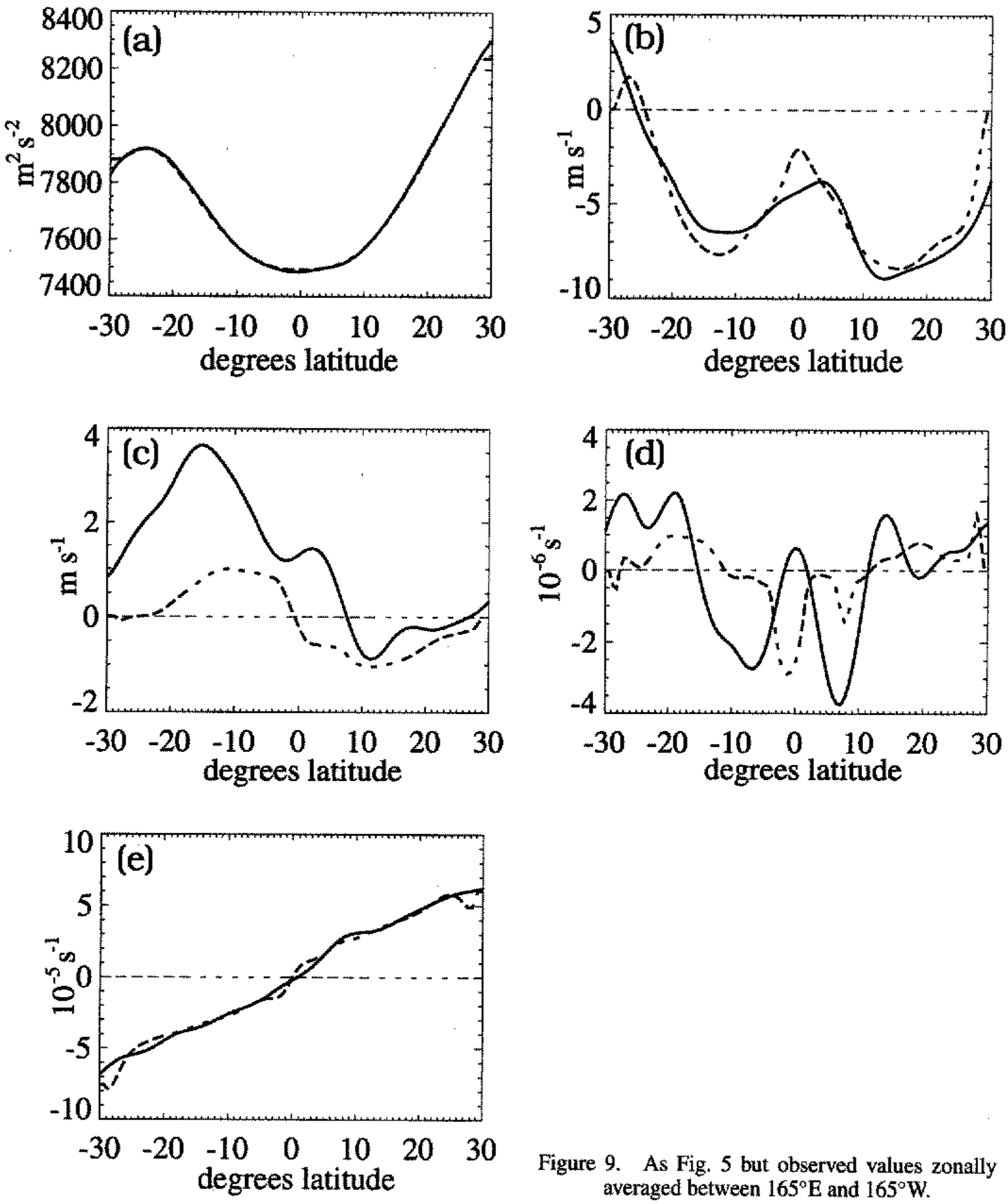

Figure 9. As Fig. 5 but observed values zonally averaged between 165°E and 165°W.

maximum is found a few degrees south of where it is found in the observations. Because the simulated and observed meridional winds are in good agreement, the convergence (Figs. 5(d) and 6(d)) is also well simulated, although it is a little too strongly simulated in both cases. For the east Pacific case (Fig. 5(d)) the convergence is located slightly south of where it is seen in the observations. Because of the strong and northwardly displaced westerly wind maximum in the simulations, the zero absolute-vorticity line is poleward of its observed location, and the absolute vorticity is stronger than observed on the cyclonic shear side. This transition from values of η that are excessively low to values that are too high occurs over a few degrees of latitude, resulting in an unrealistically large absolute-vorticity gradient in the region.

The results of the simulation made using the July mean 925 mb geopotential from the west Indian Ocean do not agree nearly as well with observations as the cases just discussed. There is some broad agreement between the simulated and observed zonal wind (Fig. 7(b)); however, there is a critical difference in the vicinity of the equator where the simulated zonal wind is substantially more easterly (and/or less westerly) between about 10°S and 10°N. This has a profound impact on the simulated meridional wind (Fig. 7(c)) resulting in an extremely strong northward maximum and, associated with it, a very unrealistic convergence maximum (Fig. 7(d)). The very broad agreement between the simulated and observed zonal wind is reflected in rough agreement between the simulated and observed absolute vorticity (Fig. 7(e)). Several differences can be seen, similar to those in the two cases previously considered. Specifically, the simulated absolute vorticity is too weak on the anticyclonic shear side of the westerly maximum located in the northern hemisphere and there is a considerable gradient in the absolute vorticity near the same westerly wind maximum.

Somewhat better agreement between the simulation and the observations for the Indian Ocean case is achieved (Fig. 8(a) and (b)) by including the observed latitude dependent zonal pressure gradient force in the zonal momentum equation (7). This force is directed eastward and thus it opposes the westward force owing to the northward divergent flow through regions where the absolute vorticity is negative. Thus, it decreases the strength of the easterly flow between 10°S and 10°N, including the ageostrophic flow between the equator and the $\eta = 0$ contour. The reduction in the ageostrophy of the zonal flow is associated with a reduction in the strength of the meridional divergent flow (20)–(22). In spite of this improvement, the zonal flow is still too easterly near the equator and the meridional response still excessively strong. We suspect that in order to obtain better agreement between the simulation and the observations, it is necessary to include the advection of zonal momentum by the zonal flow which, observations show, is substantial (TW).

The (observed) collocation of the $\eta = 0$ contour and the divergent wind maximum warrants consideration of this region using the present model, even though the low-level flow in this region is almost certainly controlled by processes on larger longitudinal scales than considered here. Better agreement between any simulation and observations may not be possible until these considerations are taken into account. These ideas will be investigated in future work using a two-dimensional formulation of the boundary layer model.

For the final case, the model is forced using the July mean 925 mb geopotential from the central Pacific where, in contrast to the cases examined previously, the cross-equatorial pressure gradient is nearly zero. Comparing the results from this experiment with observations allows us to illustrate several important differences in the relationship between the convection and the boundary layer dynamics for the cases of strong and weak cross-equatorial pressure gradients.

The simulated zonal wind (Fig. 9(b)) closely resembles the observed; there is only a slight difference in the strengths and locations of the easterly minima found near the equator. The interesting differences between the simulation and observations occur in the meridional wind (Fig. 9(c)) and the divergence (Fig. 9(d)); note that the divergence is approximately an order of magnitude weaker in this case compared to the other cases examined. The simulated meridional wind is northerly in the northern hemisphere and southerly in the southern hemisphere, and this flow is associated with weak convergence located on the equator. In contrast, the observed meridional wind shows stronger southerly winds in the southern hemisphere, and the transition from southerlies to northerlies is located in the northern hemisphere. This distribution in the strength of the observed meridional wind is associated with two somewhat weak convergence centres that straddle the equator,

one near 5°N and the other near 10°S. These convergence maxima are collocated with convection maxima (e.g. TW).

If the convection was dynamically determined in the central Pacific, as it appears to be in regions where there is a substantial cross-equatorial pressure gradient, it would be centred on the equator, where the simulation shows weak convergence. In fact, a convective minimum is observed on the equator, with convective maxima lying several degrees to the north and south. We conclude that processes other than dynamically determined convergence in the boundary layer are responsible for determining the meridional location of convection in the central Pacific Ocean. Note, this implies that in this case, the observed collocation of convection and (weak) convergence in the boundary layer is a result of a positive feedback between convection and convergence (Waliser and Somerville 1994), or convergence being determined by the convection rather than visa versa, as we believe is true for the regions where there is a substantial cross-equatorial pressure gradient force.

Furthermore, the outgoing long-wave radiation (OLR) and divergent circulation fields indicated that, in spite of the fact that the SSTs were several degrees lower, convection was stronger in these regions than the central Pacific region. This is indicated by the observation that OLR values are comparable in the central Pacific, east Pacific and Atlantic regions, and thus convection should be comparably strong in all three regions. However, the convergence is roughly half as strong in the central Pacific region as it is in the east Pacific and Atlantic regions.

Observations by Zebiak (1990) are consistent with these arguments and are also generally supportive of the boundary layer modelling approach that we have used for this study. Zebiak looked at the question of what forces the low-level flow in the tropical Pacific:

(i) convective heating;
(ii) hydrostatic adjustment to the underlying SST distribution.

In regions where convective forcing is of prime importance, a Gill (1980) type modelling approach, in which the atmospheric circulation is viewed as a simple baroclinic response to imposed (convective) heating, is appropriate. In regions where hydrostatic adjustment is of prime importance, a boundary layer type model is appropriate (e.g. Wang and Li 1993). Zebiak concluded that, in general, both forcing mechanisms appeared to be important. He noted, however, that the structure of the SST anomalies resembled the forcing structures he calculated in the ITCZ region, implying that hydrostatic adjustment to the SST may be the most important process, at least for this region. This suggests then that the boundary layer modelling approach is appropriate for this region and is also supportive of the idea that the boundary layer dynamics determine the strength and location of convection here, rather than convection determining the boundary layer dynamics. Further evidence of the importance of boundary layer dynamics in this region is provided by numerical simulations presented by Wang and Li (1993) in which they find that it is necessary to include the Lindzen-Nigam (1987) boundary layer component in their coupled boundary layer–Gill type model in order to realistically simulate the east Pacific ITCZ.

6. Discussion and summary

Large-scale flow in the boundary layer is somewhat sub-geostrophic and thus contains a cross-isobaric component. The effect that the cross-isobaric flow has on the along-isobar flow depends strongly on the sign of the local absolute vorticity. When the absolute vorticity is locally cyclonic, cross-isobaric flow drives the along-isobar flow toward geostrophic

balance. As the flow becomes closer to geostrophic balance there is decreased cross-isobaric flow; thus there is a negative feedback, and the total flow tends toward a state close to geostrophic balance with a relatively small cross-isobaric component. On the other hand, when the absolute vorticity is locally anticyclonic, cross-isobaric flow drives the along-isobar flow away from geostrophic balance. This in turn leads to increased cross-isobaric flow; thus there is a positive feedback and the total flow tends toward a state that is more sub-geostrophic and has a significantly stronger cross-isobaric component. In this case, stability is maintained by dissipation and redistribution of mass. This is why the parcel criterion for inertial instability has important implications for atmospheric motions, even though such motions involve non-zero viscosity and depth and hence do not satisfy sufficient conditions for instability. For example, the interpretation made by TW, that the locally anticyclonic absolute vorticity is responsible for the observed acceleration of the divergent flow, is correct even though a linear analysis indicates that in all cases the flows are inertially stable.

In the midlatitudes, large areas of locally anticylonic absolute vorticity are rarely observed. The reason given in many meteorological texts is that such flow would be inertially unstable, and inertially unstable motions would mix the fluid laterally and reduce the shear until the absolute vorticity became locally cyclonic. However, as was shown in section 3, linear theory indicates that shear values much greater than f are required for inertial instability when realistic values of viscosity and fluid depth are taken into account. The results presented here indicate that well before the flow became inertially unstable, an accelerated cross-isobaric divergent flow would develop. Such a flow would be more effective at redistributing mass than the forced systems examined in this paper; this mass redistribution would carry mass out of the high-pressure centre. Since, to a large extent, the relative vorticity is proportional to the Laplacian of the geopotential in the midlatitudes, this mass redistribution is associated with vorticity redistribution out of the anticyclonic maximum, located at the high-pressure centre. Thus, the divergent flow would tend to render the flow locally cyclonic before it ever became inertially unstable.

Acknowledgements

RAT and PJW were supported by the US National Science Foundation (NSF) Grant ATM-9526030; JRH was supported by NSF Physical Meteorology Program Grant ATM-9322480. We wish to thank Harry H. Hendon and Hai-ru Chang for valuable discussions concerning various parts of this work.

References

Battisti, D. S., Sarachik, E. S. and Hirst, A. C. 1999 A consistent model for the large scale steady surface atmospheric circulation in the tropics. *J. Climate.*, in press

Charney, J. G. 1971 Tropical cyclogenesis and the formation of the intertropical convergence zone. Pp. 355–368 in *Mathematical problems of geophysical fluid dynamics. Vol. 13: Lectures in applied mathematics*. Ed. W. H. Reid, American Mathematical Society, Providence, USA

Dunkerton, T. J. 1981 On the inertial stability of the equatorial middle atmosphere. *J. Atmos. Sci.*, **38,** 2354–2364

Gill, A. E. 1980 Some simple solutions for heat-induced tropical circulations. *Q. J. R. Meteorol. Soc.*, **106,** 447–462

Harrison, D. E. and Vecchi, G. A. 1997 Westerly wind events in the tropical pacific, 1986–95. *J. Climate*, **10,** 3131–3156

Hastenrath, S. 1988 *Climate and circulation of the tropics*. Atmospheric Sciences Library, Redel, Boston, USA

Hastenrath, S. and Lamb, P. J. 1977a *Climatic atlas of the tropical Atlantic and eastern Pacific Oceans.* University of Wisconsin Press, USA

1977b Some aspects of the circulation and climate over the eastern Atlantic. *Mon. Weather Rev.*, **105,** 1019–1023

Hess, P. G., Battisti, D. S. and Rasch, P. J. 1993 The maintenance of the intertropical convergence zones and the large-scale circulation on a water covered earth. *J. Atmos. Sci.*, **50,** 691–713

Holton, J. R. 1992 *An introduction to dynamic meteorology, 3rd edition.* Academic Press, San Diego, USA

Holton, J. R., Wallace, J. M. and Young, J. A. 1971 On boundary layer dynamics and the ITCZ. *J. Atmos. Sci.*, **28,** 275–280

Lindzen, R. S. 1974 Wave-CISK in the tropics. *J. Atmos. Sci.*, **31,** 156–179

Lindzen, R. S. and Nigam, S. 1987 On the role of the sea surface temperature gradients in forcing low level winds and convergence in the tropics. *J. Atmos. Sci.*, **44,** 2418–2436

Manabe, S., Hahn, D. G. and Holloway, J. L., Jr. 1974 The seasonal variation of the tropical circulation as simulated by a global model of the atmosphere. *J. Atmos. Sci.*, **31,** 775–805

Pike, A. C. 1971 The intertropical convergence zone studied with an interacting atmosphere and ocean model. *Mon. Weather Rev.*, **99,** 469–477

Ramage, C. S. 1974 Structure of an oceanic near-equatorial trough deduced from research aircraft traverses. *Mon. Weather Rev.*, **102,** 754–759

Sadler, J. 1975a The monsoon circulation and cloudiness over the GATE area. *Mon. Weather Rev.*, **103,** 369–387

Sadler, J. 1975b 'The upper tropospheric circulation over the global tropics'. UHMET-75-05, Department of Meteorology, University of Hawaii, USA

Tomas, R. A. and Webster, P. J. 1997 The role of inertial instability in determining the location and strength of near-equatorial convection. *Q. J. R. Meteorol. Soc.*, **123,** 1445–1482

Waliser, D. E. and Somerville, R. C. J. 1994 Preferred latitudes of the intertropical convergence zone. *J. Atmos. Sci.*, **51,** 1619–1639

Wang, B. and Li, T. 1993 A simple tropical atmospheric model of relevance to short-term climate variations. *J. Atmos. Sci.*, **50,** 260–284

Young, J. A. 1988 Boundary layer dynamics of tropical and monsoonal flows. Pp. 461–500 in *Monsoon meteorology*. Eds. C. P. Chang and T. N. Krishnamurti. Oxford University Press, UK

Zebiak, S. E. 1990 Diagnostic studies of Pacific surface winds. *J. Climate*, **3,** 1016–1031